

Thermopower of thermoelectric materials with resonant levels: PbTe:Tl versus PbTe:Na and Cu_{1-x}Ni_x

Bartłomiej Wiendlocha*

Faculty of Physics and Applied Computer Science, AGH University of Science and Technology, Aleja Mickiewicza 30, 30-059 Krakow, Poland



(Received 16 February 2018; published 9 May 2018)

Electronic transport properties of thermoelectric materials containing resonant levels are discussed by analyzing the two best known examples: copper-nickel metallic alloy (Cu-Ni, constantan) and thallium-doped lead telluride (PbTe:Tl). As a contrasting example of a material with a nonresonant impurity, sodium-doped PbTe is considered. Theoretical calculations of the electronic structure, Bloch spectral functions, and energy-dependent electrical conductivity at $T = 0$ K are done using the Korringa-Kohn-Rostoker method with the coherent potential approximation and the Kubo-Greenwood formalism. The effect of a resonance on the residual resistivity and electronic lifetimes in PbTe is analyzed. By using the full Fermi integrals, room-temperature thermopower is calculated, confirming its increase in PbTe:Tl versus PbTe:Na, due to the presence of the resonant level. In addition, our calculations support the self-compensation model, in which the experimentally observed reduction of carrier concentration in PbTe:Tl against the nominal one is explained by the presence of n -type Te vacancies.

DOI: [10.1103/PhysRevB.97.205203](https://doi.org/10.1103/PhysRevB.97.205203)

I. INTRODUCTION

Resonant energy levels may be formed by dopant atoms added to metals or semiconductors, at energy at which in the absence of neighboring atoms a bound state would be formed [1–3]. For semiconductors, this energy may be inside the valence or conduction bands, and then such a resonant level (RL) strongly distorts the electronic band structure of the host material, violating the rigid-band doping model. The problem of impurity-induced resonant levels has been known in solid-state physics since the 1950s from the early works on diluted metallic alloys (see, e.g., works of Korringa [4,5] or Friedel [6]; the literature on RLs in semiconductors is reviewed in Ref. [2]). A large interest in resonant levels among the thermoelectric community followed the work of Heremans *et al.* [7], where in the Tl-doped PbTe an increase of the thermopower and a large thermoelectric figure of merit of $zT > 1.5$ were found and ascribed to the presence of RL. Thallium-doped lead telluride itself was a widely studied material in the past [8–11], and this interest continues up to now due to its interesting thermoelectric properties, superconductivity [8,9,12], and Kondo-like anomalies in resistivity [13–15]. The idea of improving the thermoelectric properties of a material using resonant levels initiated a search for RLs in other thermoelectric materials [16–18], and improvement of thermoelectric properties was found in Sn-doped Bi₂Te₃ [19], In-doped SnTe [20], In-doped GeTe [21], and K-doped Bi-Sb [22], to mention several examples. A distinct group of materials with resonant levels is constituted by semiconductors doped with transition metals, in which magnetic interactions play an important role. Among them, we find PbTe doped with Cr [23–27], Fe [28,29], Sc [30], and Ti [2,31,32].

In this work, we focus on the transport properties and thermopower of thallium-doped PbTe, as the best-known example of the thermoelectric material with resonant level, and our motivation is to confirm from first-principles calculations that RL enhances its thermoelectric power S . As the characteristic feature of RL is the formation of a peak in the electronic density of states (DOS), arguments in favor of or against the possibility of a resonant increase of S are frequently raised. Originally [7], the increase of S in PbTe:Tl was explained in terms of DOS and effective mass enhancement. This reasoning was later supported by simplified calculations, which were based on the computed DOS function of the system in Ref. [2]. However, no direct computations of the thermopower based on the electronic transport functions were reported, to the best of the authors' knowledge. The arguments against the resonant enhancement of thermopower have been mostly based on the localization issues and possibility of an impurity-band formation [2,33]. If a narrow impurity band would be formed by the resonant impurity states, such a band could have a large thermopower S_i , but small conductivity σ_i if compared to the conductivity σ_h of the host material. In the case of a two-band system, total thermopower would be a weighted average $S \simeq (\sigma_h S_h + \sigma_i S_i)/(\sigma_h + \sigma_i)$ and a condition that $\sigma_h \gg \sigma_i$ results in $S \simeq S_h$, thus no enhancement in S would be observed. As we have shown in Ref. [33], no impurity-band-like states are formed in PbTe:Tl, in contrast, e.g., to PbTe:Ti [32,34]. In the current work we go further, computing the thermopower of PbTe:Tl from first principles, with no external parameters, and comparing to a nonresonant case of Na-doped PbTe. As a benchmark material, to test our procedures and have a possibility of comparing the semiconductor case to the “resonant” metallic system, we also study the transport properties of constantan (Cu-Ni alloy). Additionally, we discuss the carrier concentration problem in PbTe:Tl, where significantly lower hole concentrations are observed experimentally in the samples than expected from the chemical composition. This

*wiendlocha@fis.agh.edu.pl

longstanding problem is explained in the literature using two competitive models: a mixed TI valence model [13,14,35] and a self-compensation model [10,11], in which additional defects play a key role. Our computations support the self-compensation scenario, where Te vacancies act as a source of carrier compensation.

II. COMPUTATIONAL DETAILS

Full-potential electronic structure calculations were done using the Korringa-Kohn-Rostoker (KKR) multiple scattering method. Chemical disorder, induced by the doping, was accounted for within the coherent potential approximation (CPA), as implemented in the SPRKKR package [36,37]. The local density approximation (LDA) with the formula of Vosko *et al.* [38] was used for the construction of the crystal potential. Very dense k -point meshes were used [$\sim 8 \times 10^3$ \mathbf{k} points in the irreducible part of the Brillouin zone (BZ) for the self-consistent cycle; $1\text{--}100 \times 10^5$ \mathbf{k} points for the transport calculations], and the angular momentum cutoff $l_{\max} = 3$ was set. The Lloyd formula [37] was used to determine the Fermi level position. Spin-orbit interaction was included in all the calculations presented here. Crystal-structure parameters were taken from experiment: space group $Fm\text{-}3m$ (no. 225), $a = 6.46$ Å for PbTe [39], and $a = 3.57$ Å for Cu-Ni [40].

To illustrate the modifications of the electronic band structures, we have calculated the Bloch spectral density functions (BSFs) $A^B(\mathbf{k}, E)$, which are related to the configurationally averaged electron's Green functions [37,41,42]. More intuitively, $A^B(\mathbf{k}, E)$ is a \mathbf{k} -resolved density of states $n(E)$ [41] since

$$n(E) = \frac{1}{\Omega_{\text{BZ}}} \int_{\Omega_{\text{BZ}}} d^3k A^B(\mathbf{k}, E), \quad (1)$$

where Ω_{BZ} is the Brillouin-zone volume. For the ordered system, the BSF at a selected \mathbf{k} is a Dirac δ function $\delta(E - E_{\nu, \mathbf{k}})$, being zero everywhere except the points (\mathbf{k}, E) , where the electron in band ν has an energy eigenvalue $E_{\nu, \mathbf{k}}$. An integral of BSF over the energy is equal to one—each (\mathbf{k}) state is occupied by one electron (or two, due to spin degeneracy in the case of a nonmagnetic system). In this case, a set of BSFs along a selected \mathbf{k} path defines the usual dispersion relations, with peaks of $\delta(E - E_{\nu, \mathbf{k}})$ functions showing the position of the ideally sharp bands $E_{\nu}(\mathbf{k})$, with infinite lifetime of electronic states, as no scattering takes place. In a case of a disordered system, electrons are scattered, and thus BSF broadens, leading to blurring of energy bands and decreasing the electronic lifetime. Typically, due to broadening of the δ function, the BSF at a single \mathbf{k} point adopts the Lorentzian shape [1,43–45],

$$A^B(\mathbf{k}, E) = L(E) = \frac{1}{\pi} \frac{\frac{1}{2}\Delta}{(E - E_0)^2 + \left(\frac{1}{2}\Delta\right)^2}, \quad (2)$$

where Δ is the full width at half maximum (FWHM), representing the bandwidth, and E_0 is the Lorentzian peak position, which defines the band center. The electronic lifetime is then calculated as $\tau = \hbar/\Delta$. In the presence of strongly scattering impurities, which is the case of resonant impurities, the spectral

function becomes very wide and non-Lorentzian in shape, as it may even become impossible to point the energy band center. Classical examples of such systems are found among the transition-metal noble-metal alloys, such as Cu-Ni, which we invoke as a reference system in the next section.

Transport properties are studied using the Kubo-Greenwood formalism [46,47], as formulated for the KKR-CPA method by Butler [44,48] and implemented in the SPRKKR package by Ebert *et al.* [36,37,49,50]. This combination of the KKR-CPA method and Kubo formalism is a very powerful tool dedicated to study the electronic structure and transport properties of random alloys, and allows one to calculate the zero-temperature energy-dependent electrical conductivity $\sigma(E)$ of the system (usually called the transport function) with no adjustable parameters. Thanks to the use of Green functions and scattering path operators, unlike the Boltzmann approach, it does not require the existence of sharp, well-defined bands. Thus, it is best suited to study the systems with resonant impurities, where such well-defined bands may not exist. This formalism was successfully applied to study the transport properties of various metallic alloys, such as $3d$ magnetic systems [51,52], noble-metal–transition-metal alloys containing d resonances [53,54], or, recently, the Heusler alloys [50]. It also allows one to include the so-called vertex corrections [49] (“scattering-in” terms), which are neglected in the Boltzmann approach.

In this work, computations of $\sigma(E)$ were done with an energy step of 0.1 mRy and on a very fine k -point mesh in the Brillouin zone, with convergence tested on 2–3 times denser meshes. For the Cu-Ni metallic alloy, convergence on a 142^3 k -point mesh was obtained. For the TI-doped PbTe, 168^3 k -point mesh was optimal, whereas for the Na-doped system, especially near the valence band (VB) edge, the number of \mathbf{k} points had to be increased up to 363^3 (10^7 points in the irreducible part of the Brillouin zone). For PbTe, in the present paper, we limit our discussion to the transport properties of p -type material in a carrier concentration range $p < 10^{21}$ cm $^{-3}$ and for temperatures up to room temperature. In this case, it was sufficient to calculate the transport function in the range $-0.7 < E < 0$ eV (energy range of $27 k_B T$), where energy zero is at the valence band edge. In fact, in PbTe:TI, the thermopower is linear with T up to 500–600 K, i.e., there is no need to take into account the bipolar conduction effects at room temperature. For the Cu-Ni alloy, we took the energy range $-0.6 < E - E_F < 0.6$ eV, which was also more than sufficient to obtain convergent thermopower values for energies around the Fermi energy, E_F .

Once the transport function $\sigma(E)$ is obtained, the Seebeck coefficient is calculated as [3]

$$S = -\frac{1}{eT} \frac{L^{(1)}}{L^{(0)}}, \quad (3)$$

where

$$L^{(n)} = \int dE \left(-\frac{\partial f}{\partial E} \right) (E - \mu)^n \sigma(E). \quad (4)$$

In the formulas above, e is the electronic charge and μ is the temperature-dependent chemical potential, computed independently for each studied carrier concentration.

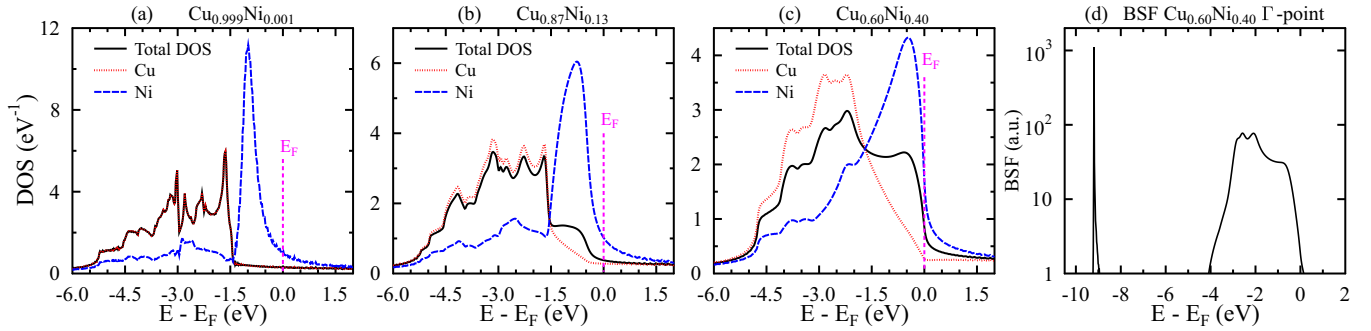


FIG. 1. (a)–(c) Calculated density of states (DOS) of $\text{Cu}_{1-x}\text{Ni}_x$ alloys. (d) Bloch spectral function of $\text{Cu}_{0.60}\text{Ni}_{0.40}$ at the $\Gamma = (0,0,0)$ \mathbf{k} point.

III. RESULTS AND DISCUSSION

A. Benchmark system: Cu-Ni

To put our results in a broader context and to test our methodology, we start with a brief analysis of a canonical example of a system containing a resonant level, which is constant. This copper-nickel (Cu-Ni) alloy, which is used to produce thermocouple wires, was one of the first materials in which the formation of RL was observed, and the proper description of its electronic structure was among the first successes of CPA theory of random metallic alloys [1]. As so, its electronic structure and transport properties were studied in a number of works, e.g., [43,55,56]. Also, analysis of the constant case allows one to highlight some important differences between the metallic and semiconducting resonant systems. We focus on the $\text{Cu}_{0.60}\text{Ni}_{0.40}$ composition, at which the alloy is paramagnetic and has a very good thermoelectric performance.

Figure 1 shows the total and component density of states of the Cu-Ni system, containing (a) 0.1%, (b) 13%, and (c) 40% of Ni. The resonant DOS peak of $3d$ orbitals of nickel is clearly seen in Fig. 1(a), and enhancement of DOS, with the increasing Ni concentration, takes place in Figs. 1(b) and 1(c). For the $\text{Cu}_{0.60}\text{Ni}_{0.40}$ case, the Fermi energy is located on the large slope of DOS, already suggesting a large thermopower of this material. Note that for a typical semiconductor, such a placement of E_F on the decreasing slope of DOS would give a positive thermopower, as in a p -type material, but in the case of constant the thermopower is negative, as we explain below.

The optimal atomic concentration of the Cu-Ni alloy, for which the thermopower has the highest absolute value near room temperature, is between 40% and 50% of Ni [40,57]. Thus, the studied material is a concentrated alloy, rather than a doped compound, but still the electronic properties of Cu-Ni alloys result from the presence of the Ni $3d$ resonance. This is especially seen in the Bloch spectral function plots. The Bloch spectral functions $A^B(\mathbf{k}, E)$, plotted as dispersion relations in high-symmetry directions for the $\text{Cu}_{0.60}\text{Ni}_{0.40}$ case, are presented in Fig. 2, with the BSF value marked by colors. As characteristic for a resonant system, we see a strongly smeared band structure below the Fermi energy due to the strong electron scattering on the $3d$ resonant states of nickel. The BSF plotted for the Γ \mathbf{k} point is presented in Fig. 1(d) and consists of two parts. The deeper, δ -like part corresponds to the bottom of the sharp, free-electron-like band, starting 9 eV below E_F in Fig. 2. The broad part, centered at -2 eV and having a

large width $\Delta \simeq 4$ eV, corresponds to the smeared bands seen in Fig. 2 at the Γ point, between -4 eV and E_F . Strong scattering, induced by the presence of the Ni $3d$ resonance, is responsible for this smearing. What is worth noting, and was highlighted in earlier works on the electronic structure of Cu-Ni alloys [43], is that in other parts of the Brillouin zone, near E_F , the band smearing is weaker and the Fermi surface still may be defined.

The calculated $T = 0$ K conductivity, along with the zoom of the density of states near E_F and thermopower S , are presented in Fig. 3. Our value of $\sigma(E_F)$, which corresponds to the residual resistivity of the alloy $\rho_0 = 1/\sigma(E_F) = 31 \mu\Omega \text{ cm}$, is consistent with the recent linear muffin-tin orbital (LMTO) calculations [56] ($\rho_0 \simeq 34 \mu\Omega \text{ cm}$), with both results larger than computed in Ref. [55] ($\rho_0 \simeq 20 \mu\Omega \text{ cm}$). However, all computed values are underestimated since the measured resistivity is $\rho_0 \simeq 45 \mu\Omega \text{ cm}$ [57], and, as discussed in [55], this larger resistivity may be caused by the formation of the Ni cluster in the samples. The first interesting observation, which is important in the context of thermopower calculations, is that conductivity is inversely proportional to the density of states, $n(E)$, $\sigma(E) \propto 1/n(E)$, due to strong s - d -like scattering on the resonance: when we move up with energy and cross E_F , we leave the resonance energy region, and electric conductivity increases. Invoking the simple free-electron formula $\sigma = \frac{ne^2\tau}{m^*}$, where n is the carriers concentration, τ is the scattering time, and m^* is the effective mass, we see that the variation in

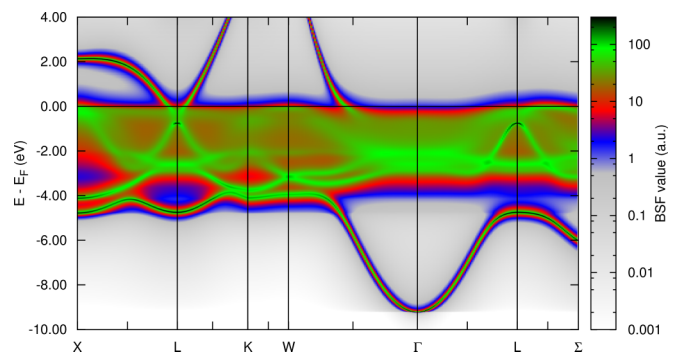


FIG. 2. The two-dimensional projections of Bloch spectral functions of $\text{Cu}_{0.60}\text{Ni}_{0.40}$ in high-symmetry directions. Here and in the following figures, the BSFs are given in atomic units (Ry^{-1}); the black color corresponds to BSF values greater than 300 a.u., i.e., 22 eV^{-1} .

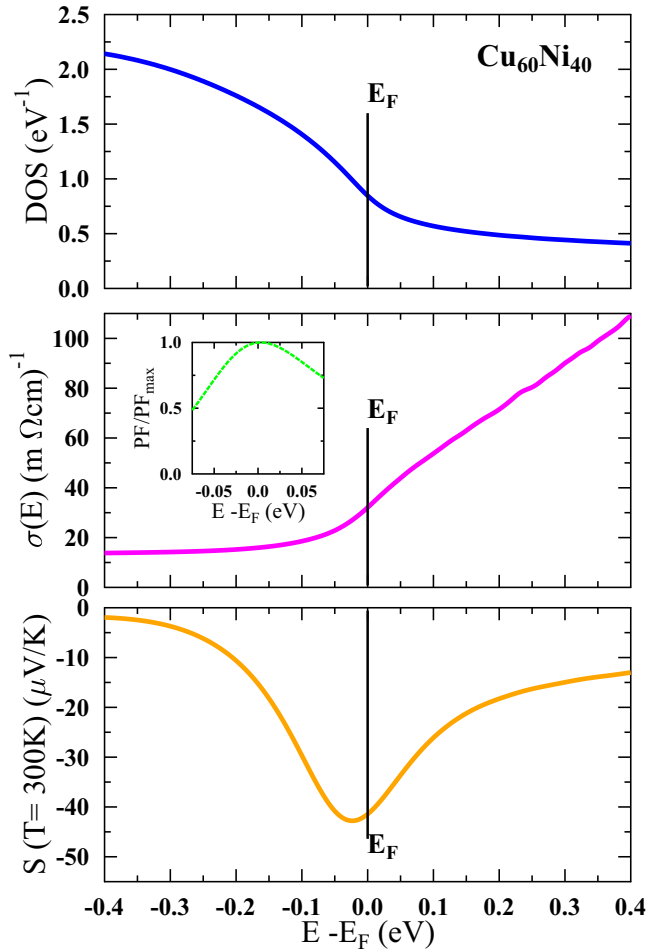


FIG. 3. Top panel: DOS of $\text{Cu}_{0.60}\text{Ni}_{0.40}$ near the Fermi energy. Middle panel: Energy-dependent electric conductivity $\sigma(E)$ at $T = 0$ K. Bottom panel: computed thermopower S at $T = 300$ K. The inset in the middle panel shows the power factor (PF) normalized by the maximum PF, which was found at $E \simeq E_F$.

$\sigma(E)$ is mostly controlled by the variation of the electronic scattering time τ since carrier concentration in this metallic case, both total and for s -like states, does not vary that much near E_F . When the electron energy increases, by leaving the resonance energy region, we increase τ and $\sigma(E)$. This increasing conductivity function results in a negative value of the thermopower since $S \propto -d \ln \sigma(E)/dE$ [3] (Mott formula). This characteristic $\sigma(E) \propto 1/n(E)$ feature of the noble-metal–transition-metal alloys was discussed before in similar “resonant” systems, such as Ag-Pd or Au-Pd alloys [45,54,58].

It is worth noting that the computed thermopower, shown in the bottom panel of Fig. 3, as well as the power factor $\text{PF} = S^2\sigma$, plotted in the inset, show that the Fermi level is almost at the ideal position, which maximizes both S and PF. Thus, if one wishes to further optimize the thermoelectric properties of constantan, other techniques than tuning of the carrier concentration (already difficult for this metallic case) have to be applied. Recently [59], scattering on the nanoscale twin boundaries was shown to improve the thermoelectric performance of Cu-Ni.

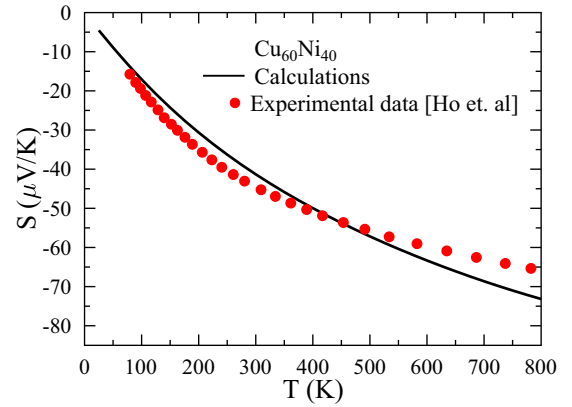


FIG. 4. Thermopower of $\text{Cu}_{0.60}\text{Ni}_{0.40}$ as a function of temperature. Experimental data after Ho *et al.* [57].

The experimental values of the thermopower of $\text{Cu}_{0.60}\text{Ni}_{0.40}$ as a function of temperature [57] and comparison with our calculations are shown in Fig. 4. The agreement between calculations and experiment is very good; room temperature values are $S_{\text{calc}} = -42 \mu\text{V/K}$, $S_{\text{expt}} = -45 \mu\text{V/K}$. S_{calc} and S_{expt} start to deviate above $T = 600$ K, but still, up to $T = 800$ K, the agreement between calculations and experiment is better than 10%. This shows that the thermoelectric properties of constantan are primarily determined by the ground-state transport function $\sigma(E)$, and due to the strong scattering on the resonant level, the electron-phonon scattering effects, neglected here, are of less importance. This is also justified by the small temperature dependence of the measured electrical resistivity of the Cu-Ni alloy since in the temperature range 0–1000 K resistivity changes are less than 5% [57]. Similar very good accuracy of the calculated thermopowers was previously reported in the literature for the already-mentioned systems: Ag-Pd and Au-Pd [45,54]. After successful determination of the thermopower of the resonant metallic alloy, a similar approach will be applied to a more difficult semiconductor case.

B. PbTe:TI versus PbTe:Na and Cu-Ni

1. Carrier concentration problem

Before addressing the thermoelectric transport properties of TI-doped PbTe, we have to discuss the problem of carrier concentration p in this system since thermopower critically depends on p . TI, a group-III element, is expected to be a monovalent acceptor TI^+ , when substituted for a group-IV element Pb, which is Pb^{2+} in PbTe. Thus, TI should deliver one hole per each substituted Pb atom. Band structure calculations in current and previous works [33,60–63] confirm this expectation. What is worth noting here is that in all these works, although different exchange-correlation potentials were used, the TI resonant state developed in a similar energy range, starting from the edge of the valence band. Although TI is not a simple rigid-band-like acceptor, the number of holes below the VB edge in the computed density of states corresponds to the TI^+ state. The mechanism of the monovalent TI doping involves the creation of two resonantlike levels [2,33,61]: a “hyperdeep” level, located about -5.5 eV below E_F , and

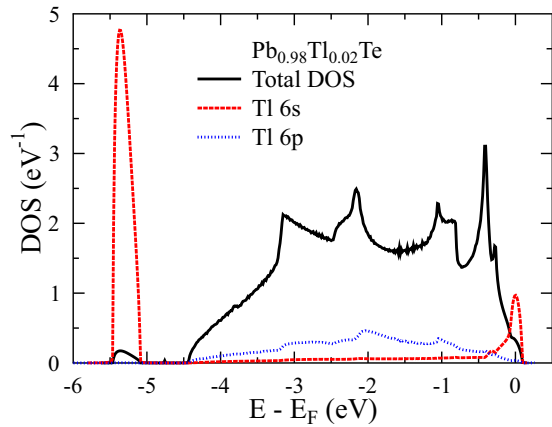


FIG. 5. Calculated densities of states (DOS) of $\text{Pb}_{0.98}\text{Tl}_{0.02}\text{Te}$: total DOS (per formula unit) and partial DOS of Tl $6s$ and $6p$ states (per Tl atom) with two resonant DOS peaks, around -5.5 eV and near the valence band edge.

the second resonant level near the valence band edge, which determines the transport properties of the system. The DOS of $\text{Pb}_{0.98}\text{Tl}_{0.02}\text{Te}$ in a broad energy range, showing both RLs, is presented in Fig. 5. Three valence electrons of Tl ($6s^26p^1$), in a simplified picture, now occupy a hyperdeep state (first $6s$ electron), the main valence band (one $6p$ electron), and the resonant state near the VB edge (second $6s$ electron). Importantly, by forming the hyperdeep state, separated by a gap from the valence band (see Fig. 5), Tl additionally bounds one electronic state, transferred from the main VB and being mostly of Te $6p$ character. Thus, effectively, by replacing the Pb atom with Tl, the valence band of PbTe is left with one electron less, making Tl a monovalent Tl^+ acceptor. This mechanism of doping via creation of the hyperdeep state is similar to what was found in Sn-, In-, and Ga-doped bismuth [64].

In various experimental studies of Tl-doped PbTe, carrier concentrations in the range $4\text{--}14 \times 10^{19} \text{ cm}^{-3}$ were reached [7,12,60], being always lower than the nominal ones and temperature dependent. In 2% Tl-doped PbTe, which has a nominal carrier concentration of $p = 3 \times 10^{20} \text{ cm}^{-3}$, the measured low-temperature ($T \leq 77$ K) Hall carrier concentration was typically near $p \simeq 1 \times 10^{20} \text{ cm}^{-3}$ [10,11,65]. At room temperature, an even lower value was noticed: $p \simeq 5 \times 10^{19} \text{ cm}^{-3}$ [7,65]. Higher carrier concentrations were reached in Ref. [60], i.e., $p \simeq 1.3 \times 10^{20} \text{ cm}^{-3}$ at $T = 77$ K and $1 \times 10^{20} \text{ cm}^{-3}$ at $T = 300$ K, most likely due to a different synthesis procedure.

Two models are discussed in the literature to explain the discrepancy between the nominal and observed carrier concentrations, at least for the low-temperature region, where any temperature-dependent phonon-scattering effects should not influence the Hall resistivity measurement. First is the mixed Tl valence model [13,14,35] and second is the so-called self-compensation model [10,11], in which defects are expected to partly compensate the acceptor behavior of Tl impurity. The main idea of the first model is that above a critical concentration, which is of the order of 0.3%, Tl in PbTe exists in both Tl^+ and Tl^{3+} states, where Tl^{3+} acts as an electron donor against Pb^{2+} , partly compensating the acceptor behavior of

Tl^+ . This model further assumes that the Tl^+ and Tl^{3+} energy levels are close, and Tl behaves as a rigid-band-like impurity, which does not disturb the PbTe valence band. However, x-ray photoelectron spectroscopy (XPS) measurements [66] contradict the mixed-valence model by showing that Tl exist in only one charge state in PbTe. Also in the more recent x-ray absorption near-edge structure (XANES) and extended x-ray absorption fine-structure (EXAFS) measurements [65,67], Tl was found to be only in a single Tl^+ state, with no signatures of Tl^{3+} . Furthermore, the formation of Te vacancies which accompany Tl in PbTe was reported there, giving support to the self-compensation model. An independent hint that the Te vacancies play an important role in controlling the carrier concentration in this system comes from the studies on Tl-doped PbTeS alloys [60]. By alloying the tellurium site with sulfur, different (and larger) carrier concentrations were reached in 2% Tl-doped samples, which may be naturally explained by a different concentration of anion vacancies. Moreover, the fact that Tl acts as a resonant impurity contradicts the assumption of its rigid-band-like behavior used in the mixed-valence model. Band structure computations show that to form a Tl^{3+} state, the second $6s$ electron of thallium would have to be excited from the hyperdeep energy level, which is located -5 eV below E_F [33,61], thus Tl^+ and Tl^{3+} energy levels are strongly separated. All these observations favor the self-compensation model, where defects, most likely the n -type Te vacancies, should be responsible for the reduction of hole concentrations in Tl-doped PbTe. This model will be verified below and used in further calculations in order to properly place E_F for the transport computations.

2. Electronic structure

Figure 6 shows the computed densities of states of $\text{Pb}_{0.98}\text{Tl}_{0.02}\text{Te}$, $\text{Pb}_{0.98}\text{Tl}_{0.02}\text{Te}_{0.9934}\text{Vac}_{0.0066}$, and $\text{Pb}_{0.99}\text{Na}_{0.01}\text{Te}$. Te vacancy is confirmed to act as a double electron donor, and its concentration in Fig. 6(b) (0.66%) was adjusted to match the carrier concentration of 10^{20} cm^{-3} , observed at low temperatures in most of the experimental studies on heavily Tl-doped PbTe [11,12,65]. The characteristic feature of the Tl-doped system is the presence of the DOS “hump” near the valence band edge, which formation is triggered by the resonant Tl $6s$ states, as was discussed before [2,33,60–62]. Tellurium vacancies only shift E_F towards the gap in the rigid-band-like manner, reducing the concentration of holes, with no visible impact on the shape of the $n(E)$ curve [cf. Figs. 6(a) and 6(b)]. This shows that, indeed, Te vacancies may act as a source of holes compensation in PbTe:Tl and are likely responsible for the lowering of the carrier concentration, detected by the Hall resistivity measurements. The temperature dependence of the carrier concentration in the samples may now be explained by the thermal generation of additional Te vacancies: to lower carrier concentration from $p = 10^{20} \text{ cm}^{-3}$ to $5 \times 10^{19} \text{ cm}^{-3}$ (as observed e.g. in Ref. [65]), an increase of the amount of Te vacancies from 0.66% to 0.83% is sufficient. It is worth recalling here that recently, the strong temperature dependence of the carrier concentration in SnSe [68] was explained in a similar way by the thermal generation of additional Sn vacancies.

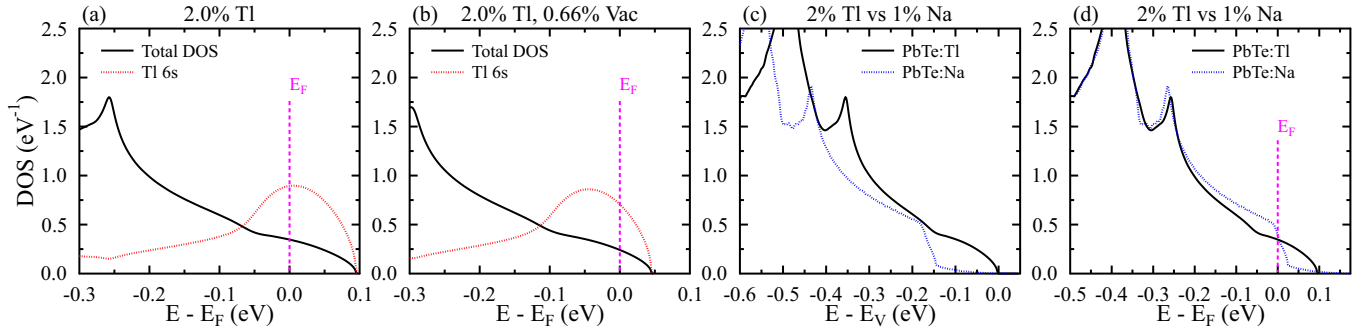


FIG. 6. (a) Calculated densities of states (DOS) of $\text{Pb}_{0.98}\text{Tl}_{0.02}\text{Te}$; (b) $\text{Pb}_{0.98}\text{Tl}_{0.02}\text{Te}_{0.9934}\text{Vac}_{0.0066}$, i.e., containing 0.66% of Te vacancies; (c),(d) 2% Tl-doped compared to 1% Na-doped PbTe, in which the zero of energy is set to (c) the valence band edge (E_V) and (d) the Fermi energy (E_F). The partial Tl 6s DOS in (a) and (b) is given per one impurity atom.

In contrast to the resonant behavior of thallium, sodium behaves as a rigid-band-like acceptor as far as the DOS modifications are concerned. This remains in agreement with earlier works [63,69]. In Figs. 6(c) and 6(d), the DOS of 1% Na-doped PbTe is compared to 2% Tl-doped PbTe to visualize the modifications of the $n(E)$ curve due to resonant doping. In Fig. 6(c), the zero of energy is shifted to the valence band edge E_V , whereas in Fig. 6(d), it is shifted to the Fermi energy E_F . This shows two important effects of Tl doping compared to Na. First is the already mentioned increase in DOS near the VB edge, which results in a reduction of the Fermi energy: to reach similar carrier concentrations in the range 10^{19} – 10^{20} cm^{-3} in Na-doped PbTe, E_F has to be about 0.1 eV deeper in the valence band than in the Tl-doped material. The second effect is the redistribution of electronic states, seen clearly in Fig. 6(d). The additional electronic states, which form the resonant “hump,” are shifted from the lower part of the DOS, towards the VB edge.

To compare modifications of the electronic bands, Bloch spectral functions for Tl- and Na-doped PbTe are shown in Fig. 7. For the Tl-doped case, we will now mainly focus on the case of 2% Tl-doped PbTe containing 0.66% of Te vacancies since this is the system which represents the experimentally studied material with low-temperature carrier concentration of 10^{20} cm^{-3} . The Fermi surface and BSFs of PbTe:Tl were discussed in more detail in our previous work [33]; here we only focus on the BSFs for the last valence band, which goes between the $L = (0.5, 0.5, 0.5)2\pi/a$ and $\Sigma = (0.375, 0.375, 0.0)2\pi/a$ points in the Brillouin zone. Due to the presence of the resonant state, the band is strongly smeared and redistribution of the electronic states is clearly seen as a “cloud” surrounding the $L - \Sigma$ band. These are strongly hybridized Tl + PbTe states, which enhance the DOS near the VB edge. It is worth recalling that no impurity band is formed by the addition of Tl [33,34], which is also in agreement with the recent experimental analysis and calculations [70]. In the nonresonant Na-doped case, presented in the bottom panel of Fig. 7, the band smearing due to the presence of Na impurities is much weaker and a sharp electronic band is still formed.

Analysis of BSFs allows one to estimate the electronic lifetime τ , which is limited by the scattering on impurities. As we mentioned in Sec. II, the width Δ of the spectral function at a selected \mathbf{k} point allows one to calculate the lifetime of the

electronic state as $\tau = \hbar/\Delta$ [1,43–45]. To analyze the shape of spectral functions and electronic lifetimes, a set of $A^B(\mathbf{k}, E)$ for 200 \mathbf{k} points along the $L - \Sigma$ direction was computed, with a very small energy step of 0.0125 mRy (0.17 meV). Figure 8 shows the spectral functions plotted for a representative \mathbf{k} point, located in 3/4 of the $L - \Sigma$ distance. Points represent computed BSF values, whereas the dashed line is a fit to a Lorentz function $L(E)$ [Eq. (2)] multiplied by 2.0, to take into account the spin degeneracy of our nonmagnetic system [71]. The fitting procedure had two parameters: Δ and E_0 .

As one can see, in the Na-doping case in Fig. 8(a), $L(E)$ almost perfectly fits the spectral function shape. In such a case, we have a well-defined band center and scattering effects may be described in the relaxation-time approximation. Fitting yields $\Delta = 4$ meV, which corresponds to $\tau = 1.64 \times 10^{-13}$ s.

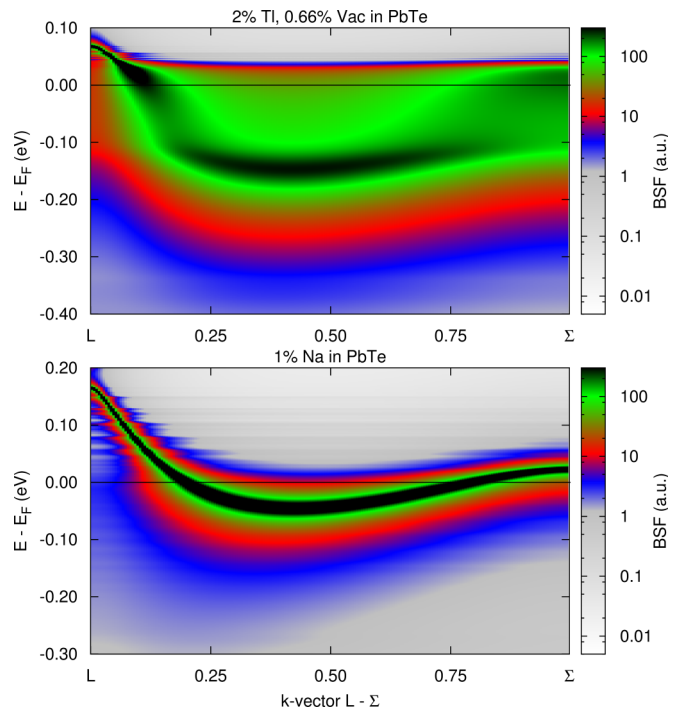


FIG. 7. The two-dimensional projection of Bloch spectral functions of $\text{Pb}_{0.98}\text{Tl}_{0.02}\text{Te}_{0.9934}\text{Vac}_{0.0066}$ (top panel) and $\text{Pb}_{0.99}\text{Na}_{0.01}\text{Te}$ (bottom panel), between the L and Σ points.

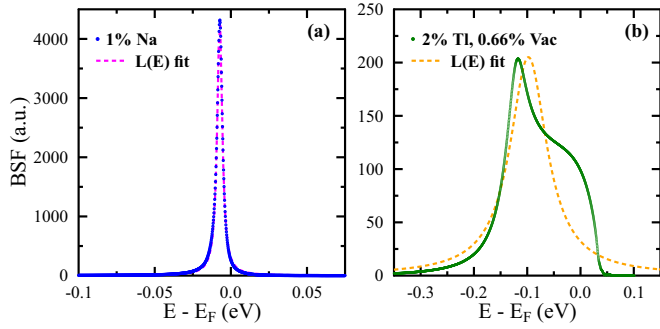


FIG. 8. Bloch spectral function of (a) $\text{Pb}_{0.99}\text{Na}_{0.01}\text{Te}$ and (b) $\text{Pb}_{0.98}\text{Tl}_{0.02}\text{Te}_{0.9934}\text{Vac}_{0.0066}$, computed for $\mathbf{k} \simeq (0.406, 0.406, 0.125)2\pi/a$, i.e., point located in 0.75 of the distance from L to Σ .

On the other hand, in the Tl-doped case in Fig. 8(b), similarly to the Cu-Ni alloy case in Fig. 1(d), BSF has a non-Lorentzian shape with a broad “shoulder” next to the peak. In this case, $L(E)$ rather poorly fits the real $A^B(\mathbf{k}, E)$ function. In the \mathbf{k} -points region between 0.1 and 0.25, and above 0.75 of the $L - \Sigma$ distance (see Fig. 7), the situation is even worse: the shoulder of BSF, appearing due to the resonant state, is even larger than the peak of the original band. It should be stressed that such a non-Lorentzian structure with a shoulder, or even two maxima in BSF, should not be confused with BSFs of two overlapping bands since the occupation of the electronic state, represented by this spectral function, is 1.0 (2.0 when including spin degeneracy), and thus corresponds to one (spin-degenerated) $|\mathbf{k}$ state.

This shows that sharp and well-defined bands do not exist in Tl-doped PbTe near the valence band edge: neither the band center nor the lifetime time can be precisely computed. As a consequence, application of the relaxation-time approximation to the computations of the transport properties would become questionable. Nevertheless, just to compare numbers, we have estimated the lifetime in PbTe:Tl based on the fitted FWHM value. The fit presented in Fig. 8(b) results in a much larger $\Delta = 84$ meV, when comparing to the Na case, resulting in a much shorter $\tau = 7.79 \times 10^{-15}$ s. The same analysis was done for all remaining \mathbf{k} points from the $L - \Sigma$ direction, and lifetimes are plotted in Fig. 9 as a function of k [Fig. 9(a)] and energy [i.e., band center E_0 in Eq. (2), Fig. 9(b)]. However, for the Tl case, one has to remember that both τ and E_0 are not well defined. For the Na case, the lifetime decreases from 10^{-12} s near the VB edge to 10^{-13} s at the bottom of the $L - \Sigma$ band. For the Tl case, τ quickly drops from 10^{-12} s near the VB edge to $\sim 10^{-14}$ s for the lower energies. Results show that for both cases, the lifetime is both \mathbf{k} and energy dependent, is strongly reduced in the presence of RL, and decreases when the energy of the electronic state is deeper in the valence band.

3. Transport properties

Thanks to using the Kubo formalism, the potential problems with relaxation-time approximation and sharp band structure are avoided, and transport properties of materials with resonant states may be studied using electronic structure calculations, with no external parameters. Zero-temperature

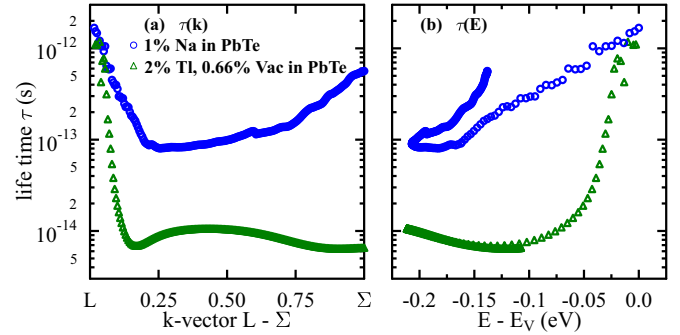


FIG. 9. Electronic lifetime τ of the valence band states in $\text{Pb}_{0.99}\text{Na}_{0.01}\text{Te}$ and $\text{Pb}_{0.98}\text{Tl}_{0.02}\text{Te}_{0.9934}\text{Vac}_{0.0066}$ along the $L - \Sigma$ direction, as a function of the (a) k vector and (b) energy. In (b), the energy scale was shifted relative to the valence band edge, E_V .

transport functions $\sigma(E)$ of $\text{Pb}_{0.98}\text{Tl}_{0.02}\text{Te}_{1-y}\text{Vac}_y$ for the three y cases, $y = 0.00$, $y = 0.66\%$, and $y = 0.83\%$, are collected in Fig. 10. Vacancy concentrations of $y = 0.66\%$ and $y = 0.83\%$ correspond to carrier concentrations $p = 1 \times 10^{20} \text{ cm}^{-3}$ and $p = 5 \times 10^{19} \text{ cm}^{-3}$, most often observed in 2% Tl-doped samples at low and room temperature, respectively. In addition, one example of the sulfur-substituted PbTe:Tl system was considered, $\text{Pb}_{0.98}\text{Tl}_{0.02}\text{Te}_{0.92}\text{S}_{0.08}$. Several Tl-doped PbTeS alloys were studied in detail by Jaworski *et al.* [60], and the same large thermopower as in Tl-doped PbTe was found in those systems, with an additional improvement of the thermoelectric performance due to the alloy scattering of phonons. Also, substitution of sulfur on the Te site allowed one to reach different (larger) carrier concentrations in the samples [60], which we attribute to compensation of some of the Te vacancies by S. The zero of energy for all computed curves was set to the valence band edge E_V in Fig. 10, and Fig. 10(b) shows a zoom near the band edge. Transport functions for particular compositions differ considerably at lower energies, $-0.7 < E < -0.3$ eV, and the addition of vacancies, or sulfur, on the Te site decreases $\sigma(E)$, as expected. On the other hand, near the VB edge, $\sigma(E)$ curves fall on each other. This is understood since, in this energy range, the presence of the Tl-induced resonant state strongly enhances electron scattering and additionally rigid-band-like defects (vacancy or S atoms on the Te site) do not affect conductivity further.

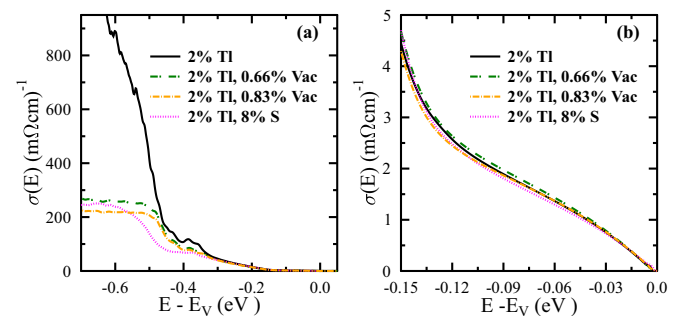


FIG. 10. Transport functions of 2% Tl-doped PbTe with Te vacancies or Te/S substitution. (b) The zoom of (a) near the VB edge, set as zero of energy.

TABLE I. Calculated and experimental residual resistivities ρ_0 of various doped PbTe samples of the formula $\text{Pb}_{1-x}\text{A}_x\text{Te}_{1-y}\text{B}_y$, where $A = \text{TI}$ or Na , and $B = \text{Vac}$ or S . Concentration of Te vacancies (y) was chosen to fit the nominal carrier concentration to the low-temperature Hall measurements, given in Refs. [11,12,65,72]. The computed resistivities are convergent to about $0.01 \text{ m}\Omega \text{ cm}$ for TI-doped materials, and $1 \mu\Omega \text{ cm}$ ($0.001 \text{ m}\Omega \text{ cm}$) for the Na-doped case.

x TI (%)	y Vac (%)	p (cm^{-3})	ρ_0^{calc} ($\text{m}\Omega \text{ cm}$)	ρ_0^{expt} ($\text{m}\Omega \text{ cm}$)
2.0	0.00	3.0×10^{20}	0.49	
2.0	0.66	1.0×10^{20}	0.85	~ 1 [11]
2.0	0.83	5.0×10^{19}	1.37	
1.6	0.49	9.1×10^{19}	0.89	0.70 ± 0.10 [65]
1.4	0.35	1.0×10^{20}	0.80	0.90 ± 0.10 [12,72]
1.3	0.31	1.0×10^{20}	0.81	0.80 ± 0.15 [72]
1.1	0.24	9.2×10^{19}	0.83	$0.77\text{--}0.95$ [35,72]
x TI	y S	p (cm^{-3})	ρ_0^{calc} ($\text{m}\Omega \text{ cm}$)	ρ_0^{expt} ($\text{m}\Omega \text{ cm}$)
2.0	8.0	3.0×10^{20}	0.54	
x Na	y S	p (cm^{-3})	ρ_0^{calc} ($\text{m}\Omega \text{ cm}$)	ρ_0^{expt} ($\text{m}\Omega \text{ cm}$)
1.0		1.5×10^{20}	0.025	0.034 [73]

Taking the conductivity value at the Fermi level, residual resistivity $\rho_0 = 1/\sigma(E_F)$ is obtained and may be compared with experimental findings. Unfortunately, in the literature, there are few results of the low-temperature resistivity measurements for 2% TI-doped samples. Data collected in Ref. [11] show that $\rho_0 \geq 1 \text{ m}\Omega \text{ cm}$ for the 2% TI-doped samples that have low-temperature carrier concentration around $1 \times 10^{20} \text{ cm}^{-3}$. Heremans *et al.* [7] measured resistivity down to 77 K, where $\rho = 2.0 \text{ m}\Omega \text{ cm}$, and extrapolation of the low-temperature part of the $\rho(T)$ curve to $T = 0 \text{ K}$ gives a similar estimation of $\rho_0 \simeq 1 \pm 0.2 \text{ m}\Omega \text{ cm}$. Extrapolation of the Hall carrier concentration measurements of Ref. [7] also gives the low-temperature carrier concentration around $\sim 10^{20} \text{ cm}^{-3}$, and thus the experimental values of both Refs. [7,11] should be compared to our 2%-TI, 0.66%-Vac case. The calculated value is then slightly lower, $\rho_0 = 0.85 \text{ m}\Omega \text{ cm}$, as shown in Table I. Since the results of the low-temperature resistivity measurements were available in the literature for several other concentrations of TI, computations of conductivity at the Fermi energy were done, and all ρ_0 values are collected in Table I. In each case, to match the nominal carrier concentration in calculations to the experimental, low-temperature Hall concentrations, an appropriate number of Te vacancies was added to the system. All computed resistivities are in the range $0.80\text{--}0.90 \text{ m}\Omega \text{ cm}$, whereas the experimental values span the range from 0.70 to $0.95 \text{ m}\Omega \text{ cm}$, with the typical uncertainty [74] around $0.10 \text{ m}\Omega \text{ cm}$. The agreement between calculations and experiment is quite good; within the error bars, almost all the computed data agree with measurements. Table I also includes resistivity data computed for $\text{Pb}_{0.98}\text{TI}_{0.02}\text{Te}_{0.92}\text{S}_{0.08}$ and $\text{Pb}_{0.99}\text{Na}_{0.01}\text{Te}$. The Te/S alloying increases resistivity in 10%. Comparing now the resistivity of TI-doped samples to PbTe doped with nonresonant Na, we see a significant increase in resistivity due to the presence of the resonant state. 1% Na-doped PbTe has $\rho_0 = 25 \mu\Omega \text{ cm}$, which is 30 times lower than ρ_0 of TI-doped samples, which is a natural consequence of the longer electronic lifetimes in the nonresonant doping case. Importantly,

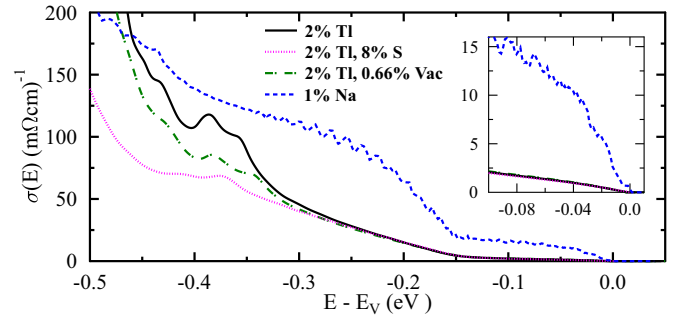


FIG. 11. Transport function of 1% Na-doped PbTe compared to 2% TI-doped PbTe. Inset shows the zoom near the VB edge, set as zero of energy.

the computed value of ρ_0 in PbTe:Na is again in a reasonable agreement with experiment since measurements give $\rho_0 = 34 \mu\Omega \text{ cm}$ [73]. The agreement is not perfect, but taking into account the small absolute values of these resistivities and the fact that the measured ρ_0 may contain additional contributions, e.g., from scattering on grain boundaries or Na precipitates, it is considered as satisfactory. The possible sources of inaccuracy of ρ_0 calculations are discussed in the next paragraph.

The general agreement of the theoretical and experimental ρ_0 values in PbTe:TI independently prove the existence of the resonant state on TI atoms in PbTe, and its correct description in the KKR-CPA formalism. The position of the TI resonance with respect to the valence band edge also seems to be well described by our LDA calculations since a 20 meV decrease (increase) of E_F changes computed ρ_0 in +50% (−25%), respectively. Without the resonant state, it would be difficult to explain the significant difference between ρ_0 of the Na- and TI-doped cases, with the 30-times increased resistivity of TI-doped samples, when comparing to Na. This shows that an analysis of the residual resistivity may be used in future studies as an important indicator of whether transport properties of the material are governed by the resonant state. This certainly requires the availability of a set of a good-quality samples doped with different impurities, in which the scattering on impurities would be the dominating source of resistivity. Moreover, our calculations of ρ_0 indirectly support the idea of carriers compensation by the Te vacancies in PbTe:TI since without the shift of the Fermi level, induced by n -type vacancies, the calculated residual resistivities would be about twice as small.

Transport function of $\text{Pb}_{0.99}\text{Na}_{0.01}\text{Te}$ in a broad energy range was computed for thermopower calculations and is compared to the TI-doped materials in Fig. 11. For lower energies, outside of the TI-resonance region, the difference in conductivity between the TI and Na cases becomes less pronounced. But since these compounds have different E_F and different carrier concentrations, it is better to compare $T = 0 \text{ K}$ “nominal” mobilities, $\mu = \sigma/(pe)$, where p is the carrier concentration and e is the elementary charge. For 1% Na-doped PbTe, we get $\mu = 1670 \text{ cm}^2/(\text{Vs})$, while for 2% TI, 0.66% Vac, we get $\mu = 73 \text{ cm}^2/(\text{Vs})$. The reduction in mobility due to the presence of resonance is strong and responsible for the observed resistivity enhancement. However, at elevated temperatures (which we are not able to discuss here from

first-principles calculations), the difference in mobility will not be that large since the electron-phonon scattering will have a much stronger effect on the Na-doped system than on the Tl-doped one, where resistivity is already large. A similar situation is found in the Cu-Ni alloy case, although there the resistivity is almost completely temperature independent. Comparing measurements for 1% Na- and 2% Tl-doped PbTe [7,75] at $T = 300$ K, the ratio of mobilities is only about 2:1 [120 vs $55 \text{ cm}^2/(\text{Vs})$] and decreases further for higher temperatures, reaching 1.7:1 at $T = 600$ K [$27 \text{ cm}^2/(\text{Vs})$ in PbTe:Na vs $16 \text{ cm}^2/(\text{Vs})$ in PbTe:Tl]. This smaller sensitivity of “resonant” samples to the phonon scattering of carriers makes it possible to obtain large power factors at elevated temperatures, even though the reduction of mobility due to resonant scattering is strong.

Before analyzing the thermopower, let us compare conductivity of the two resonant systems, i.e., metallic $\text{Cu}_{0.60}\text{Ni}_{0.40}$ alloy and semiconducting PbTe:Tl. Comparing Fig. 3 with Fig. 10, we immediately see the qualitative difference between these two cases. In PbTe:Tl, conductivity is proportional to the density of states, $\sigma(E) \propto n(E)$, while in constantan, we had $\sigma(E) \propto 1/n(E)$. Looking again at the basic formula $\sigma = \frac{ne^2\tau}{m^*}$, in the PbTe:Tl case, energy dependence of σ is controlled by the change in the number of charge carriers, n , which increases more rapidly, while E is going deeper into the valence band than the τ decreases. This results in the proportionality of the $\sigma(E)$ and $n(E)$ functions [76] and shows that the scattering of electrons due to the presence of an s -like resonant level in PbTe:Tl is not such a dominant factor, as in the case of RL on Ni in the Cu-Ni alloy. In constantan, s -like carriers are strongly scattered on a $3d$ resonance, and thus $\sigma(E)$ drops when E enters the resonant DOS region in Fig. 3. This explains the difference in sign of the thermopowers of constantan, which is negative, and PbTe:Tl, which will be positive.

Finally, the computed transport functions $\sigma(E)$ were used to calculate the room-temperature thermopower, using Eq. (3), for each of the $\sigma(E)$ functions, presented in Figs. 10 and 11. To generate the Pisarenko curves presented in Fig. 12 (thermopower as a function of the carrier concentration) for each studied composition, E_F was rigidly moved to cover the hole concentration range up to $3 \times 10^{20} \text{ cm}^{-3}$. This “local” rigid-band model may be justified for a Tl-doped system for carrier concentrations $p \gtrsim 2-3 \times 10^{19} \text{ cm}^{-3}$, since in real samples the differences in p for the fixed 2% Tl concentration occur due to the presence of a different number of Te vacancies, as we reasoned out above. As we have seen in Fig. 10, small variations in the vacancy concentration do not change the $\sigma(E)$ functions in the energy range that is important for the thermopower calculations at room temperature. This leads to the overlapping Pisarenko curves for $\text{Pb}_{0.98}\text{Tl}_{0.02}\text{Te}_{1-y}\text{Vac}_y$ in Fig. 12, which *a posteriori* justify the local rigid-band model. Also, the computed thermopower of the doubly, 2% Tl-, 8% S-doped PbTe overlaps with these results, reproducing the experimental observation of similar thermopowers of PbTe:Tl and PbTeS:Tl [60].

For the Na-doped case, we expect that computations performed for 1% Na-doped PbTe should be representative for concentrations near $p \sim 10^{20} \text{ cm}^{-3}$, i.e., near the nominal concentration of the system. For lower concentrations (below $p \sim 10^{19} \text{ cm}^{-3}$), which correspond to much lower nominal

Na concentration, we expected deviations of the experimental thermopower from S predicted by the rigid-band model, which is using $\sigma(E)$ of the 1% Na-doped system. Since this carrier concentration range is not important for the comparison with PbTe:Tl, additional calculations done for 0.5% Na-doped PbTe are discussed in the appendices.

The first and most important conclusion from Fig. 12 is that the computed thermopower of Tl-doped PbTe is strongly enhanced compared to Na-doped PbTe. For hole concentrations reached in practice ($2-11 \times 10^{19} \text{ cm}^{-3}$ at room temperature), the computed thermopower enhancement $\Delta S = S_{\text{PbTe:Tl}} - S_{\text{PbTe:Na}}$ at $T = 300$ K is from ~ 150 to $\sim 60 \mu\text{V/K}$, whereas in experiment it oscillates around $\Delta S \simeq 70 \mu\text{V/K}$, with some variations from sample to sample. Comparing absolute values of S in this carrier concentration range, for PbTe:Tl the calculations predict the thermopower from 250 to $160 \mu\text{V/K}$, whereas experiment gives $S \sim 120-150 \mu\text{V/K}$. For Na-doped PbTe, we have $S_{\text{calc}} = 85-100 \mu\text{V/K}$ and $S_{\text{expt}} = 85-50 \mu\text{V/K}$, as presented in Fig. 12. Thus, calculations for both systems overestimate the thermopower, but the systematic error is similar for both cases, reasonably predicting the relative enhancement of S and confirming the increase of the thermopower due to the presence of the Tl resonant state.

4. Sources of inaccuracy

We suspect several main sources of the overestimation of the computed thermopower. First we note that earlier attempts (e.g., [69,80]) to calculate the thermopower of p -type PbTe from first principles resulted in even larger overestimations of S compared to our results for the Na-doped material. For example, Ref. [80], by using the rigid-band model and the constant scattering time approximation, predicts $S = 120 \mu\text{V/K}$ at $p = 10^{20} \text{ cm}^{-3}$ and $T = 300$ K, whereas our computation gives $S = 97 \mu\text{V/K}$, which is closer to $S_{\text{expt}} \sim 55 \mu\text{V/K}$. This shows that in PbTe, the first-principles transport properties modeling is generally difficult, which is likely associated with the inaccuracy of the local density methods for the treatment of the exchange and correlation effects. Apart from the possible inaccurate description of the electron scattering process, overestimation of the Seebeck coefficient may be related to two band-structure-related and interconnected factors. These are an inaccurate band curvature (overestimating the effective masses) and an underestimated energy separation of the tops to the valence band at the L and Σ points, making PbTe a multivalley material at too low carrier concentration. These two factors are strongly connected since the band extrema at the L and Σ points belong to the same $L - \Sigma$ band (see Fig. 7), and thus too high energy position of the top at Σ will be correlated in a change of the geometry of this band at other energies, which influences its effective mass. In a very recent theoretical work [81], it was shown that by using the hybrid functionals (not available in our KKR-CPA studies), one can obtain the thermopower of p -type PbTe above 10^{19} cm^{-3} in a better agreement with experiment than when using other functionals. Hybrid functionals predicted both larger energy separation between the tops of the valence band at the L and Σ points as well as a sharper band shape near the L point (which will result in a smaller effective mass, not studied in Ref. [81]).

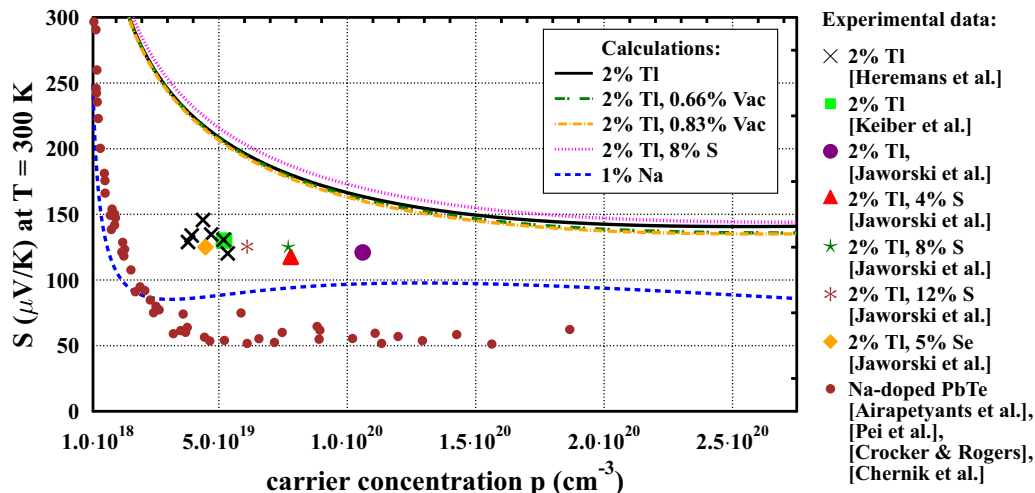


FIG. 12. Thermopower at $T = 300$ K as a function of hole concentration (Pisarenko plot) of 2% Tl-doped PbTe containing Te vacancies or Te/S substitution, compared to 1% Na-doped PbTe. Points show experimental results, as described in the legend, from Heremans *et al.* [7], Jaworski *et al.* [60], Keiber *et al.* [65], Pei *et al.* [75], Airapetyants *et al.* [77], Crocker and Rogers [78], and Chernik *et al.* [79]. As it is rather impossible to obtain 2% Tl-doped PbTe samples with $p < 10^{19}$ cm^{-3} , this part of the plot does not describe any real material, and is left only for the completeness of the plot.

Similarly as reported in other works which used nonhybrid functionals (see Ref. [82], and references therein), our calculations suffer from the Σ band position problem. In our case of PbTe:Na, E_F starts to penetrate the Σ band at $p \simeq 6 \times 10^{19}$ cm^{-3} , whereas recent experimental studies of Na-doped PbTe have shown that at least up to $p \simeq 10^{20}$ cm^{-3} , PbTe is a single-band material [82]. The Σ band shift results in a rapid increase of the computed $\sigma(E)$ function at -150 meV in Fig. 11, which gives rise to the thermopower overestimation in this carrier concentration range. At room temperature, where electronic states from the energy range of a few $k_B T$ contribute to the transport properties, the band shift will influence the computed thermopower for even lower p . This effect is hard to distinguish in the Pisarenko curve for PbTe:Tl since the $L - \Sigma$ band is blurred due to the presence of the resonant state, but may be caught for PbTe:Na. In Fig. 12, the computed room-temperature thermopower of $\text{Pb}_{0.99}\text{Na}_{0.01}\text{Te}$ stops to decrease with increasing p at around $p = 2 \times 10^{19}$ cm^{-3} , and has a characteristic plateau for larger p , with $S \simeq 85$ – 100 $\mu\text{V}/\text{K}$. The experimental thermopower, on the other hand, saturates for higher $p \geq 5 \times 10^{19}$ cm^{-3} , reaching lower $S \simeq 55$ $\mu\text{V}/\text{K}$, which is correlated with the lower Σ band position. Analysis of the effective mass, discussed in more detail in the next paragraph, also shows the overestimating trend of the LDA computations for $p > 10^{19}$ cm^{-3} . These two LDA-based problems result in an overestimated thermopower at the higher carrier concentrations range. However, as we already mentioned, this should be a systematic error, present for both PbTe:Na and PbTe:Tl, and thus should not affect the conclusion of the relative increase of the thermopower of PbTe:Tl against PbTe:Na.

Finally, in our calculations, the temperature-dependent electron-phonon scattering effects are neglected. By taking into account electron scattering due to the presence of impurities, we go one step beyond the most commonly used constant scattering time approximation. This proves to be sufficient

to confirm the resonant enhancement of the thermopower in PbTe:Tl versus PbTe:Na, but is still insufficient to compute the exact values of S . Unlike the Cu-Ni case, PbTe obviously has a temperature-dependent electrical resistivity and, by neglecting the phonon scattering effects, we expect to obtain an overestimated thermopower. This especially holds for the system where acoustic phonon scattering is strong, which is the case of PbTe at room temperature [60].

As far as the accuracy of the computed residual resistivity is concerned, in line with the shift of the Σ band towards the VB edge, our computed residual resistivity of $\text{Pb}_{0.99}\text{Na}_{0.01}\text{Te}$ was too small. On the other hand, in PbTe:Tl, the transport function is less energy dependent and, due to band blurring, less sensitive to the relative band position problem, which is correlated with the better accuracy of the calculated residual resistivities, when comparing to PbTe:Na. For both considered doping cases, ρ_0 are computed with a better accuracy than S . The first reason for that is the above-mentioned neglect of the temperature-induced scattering effects in the thermopower calculations. The second one is the propagation of error from the deeper-lying electronic states in the thermopower computations since, at $T = 300$ K, S depend on the transport function in a large energy window ($\sim 12 k_B T = 0.3$ eV). Thus, inaccuracy of the $\sigma(E)$ for the deeper energies (including states below E_F) will affect the accuracy of the thermopower calculations, not necessarily influencing the ρ_0 value at the same carrier concentration.

C. Effective mass and qualitative explanation of the thermopower enhancement

In the previous section, the resonant increase of thermopower was confirmed by direct computations of S by using the transport functions, obtained in the first-principles calculations. In this section, we would like to confront our calculations with the more intuitive and qualitative view of

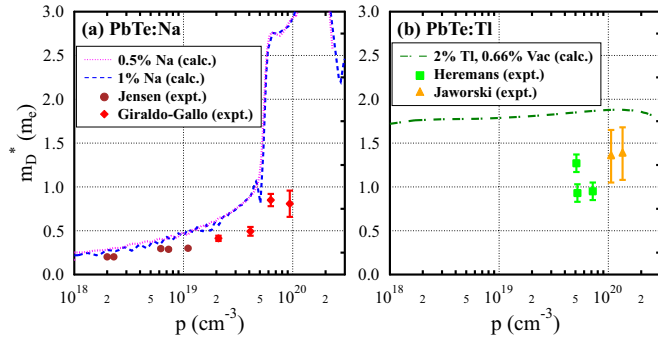


FIG. 13. Calculated DOS effective mass m_D^* as a function of hole concentration p for (a) $\text{Pb}_{0.995}\text{Na}_{0.005}\text{Te}$ and $\text{Pb}_{0.99}\text{Na}_{0.01}\text{Te}$ and (b) $\text{Pb}_{0.98}\text{Tl}_{0.02}\text{Te}_{0.9934}\text{Vac}_{0.0066}$. Points are based on the experimental measurements of Giraldo-Gallo *et al.* [82], Jensen *et al.* [83], Heremans *et al.* [7], and Jaworski *et al.* [60]. For PbTe:Na, an increase in the computed m_D^* marks the concentration $p = 6 \times 10^{-19} \text{ cm}^{-3}$, where the second valence band maximum at the Σ point is located in our LDA calculations. Above this point, the single-band effective mass picture does not apply.

resonant effect, as such arguments are usually evoked in experimental works, and discuss the effective mass in more detail. Figure 13 shows the computed density of states effective mass, m_D^* , for 0.5% and 1% Na-doped PbTe [Fig. 13(a)] and 2% Tl-doped PbTe containing 0.66% of Te vacancies [Fig. 13(b)]. The mass is calculated using the formula [84,85]

$$m_D^*(E) = \frac{\hbar^2}{m_e} \sqrt[3]{\pi^4 n(E) n'(E) / V^2}, \quad (5)$$

where $n(E)$ is the density of states (per energy and formula unit) and V is the unit-cell volume. For convenience of the reader, this formula is derived in the appendices. In PbTe:Tl, a fairly constant $m_D^* \simeq 1.75 \pm 0.1 m_e$ is obtained in the presented carrier concentration range and is enhanced, compared to PbTe:Na, where $0.25 < m_D^* < 1.0$ for $p \in (10^{18}, 6 \times 10^{19}) \text{ cm}^{-3}$. Importantly, since there is no impurity band formation in PbTe:Tl, this large DOS still corresponds to a single, but smeared band. As, in general, thermopower is proportional to m_D^* , the enhancement in m_D^* qualitatively explains the enhancement in S . This may be justified by evoking the simplest formula for the thermopower in the single-parabolic band (SPB) model in a degenerated case and constant scattering time approximation [7],

$$S = \frac{8\pi^2 k_B^2}{3eh^2} T m_D^* \left(\frac{\pi}{3p} \right)^{2/3}. \quad (6)$$

Although this formula is not directly applicable in our carrier concentration range, it explicitly shows the proportionality $S \propto m_D^*$, and was originally used in Ref. [7] to support the idea of the enhancement in S by the resonant level. The computed DOS effective mass increases rapidly in PbTe:Na above the carrier concentration $p = 6 \times 10^{-19} \text{ cm}^{-3}$, where in our calculations the Σ band starts to contribute to DOS. But there, neither the single-band formalism nor Eq. (6) may be applied, and thus our computed S does not increase rapidly above this concentration, as we have seen in Fig. 12. Figures 13(a) and 13(b) also show a comparison of the computed m_D^* to the experimental

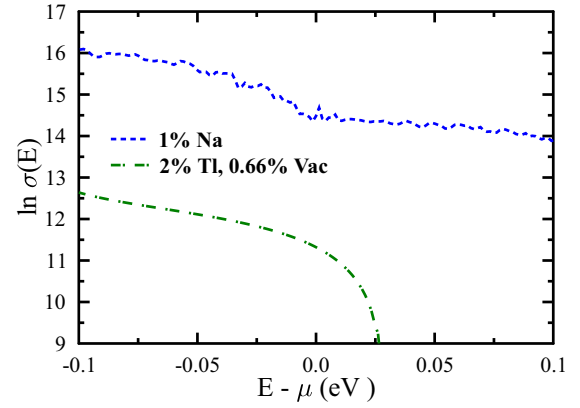


FIG. 14. Logarithm of the transport function $\sigma(E)$ as a function of reduced energy $E - \mu$ in $\text{Pb}_{0.99}\text{Na}_{0.01}\text{Te}$ and $\text{Pb}_{0.98}\text{Tl}_{0.02}\text{Te}_{0.9934}\text{Vac}_{0.0066}$. Chemical potential μ is computed at $T = 300 \text{ K}$ for the nominal carrier concentrations: $1.5 \times 10^{20} \text{ cm}^{-3}$ (Na) and $1.0 \times 10^{20} \text{ cm}^{-3}$ (Tl).

data. For PbTe:Na, we based our computation on the cyclotron effective mass measurements [86] of Giraldo-Gallo *et al.* [82] and Jensen *et al.* [83], whereas for PbTe:Tl, m_D^* was extracted from the transport measurements [87] by Heremans *et al.* [7] and Jaworski *et al.* [60]. For PbTe:Na, quite good agreement is found for lower carrier concentrations, but calculations overestimate the experimental effective mass above 10^{19} cm^{-3} since the valence band starts to flatten too early. When p reaches $6 \times 10^{-19} \text{ cm}^{-3}$, the computed m_D^* artificially increases due to the contribution from the second valence band maximum at the Σ point, whereas in reality a single band is still observed. For the PbTe:Tl case, we also observe an overestimation in the computed effective masses against the experimental ones, which correlates with the overestimated thermopower. Nevertheless, both experiment and calculations consistently predict a relative enhancement of the DOS effective mass due to the presence of the Tl resonant state, giving the qualitative and intuitive explanation for the increase in S .

The qualitative analysis in terms of the effective mass and SPB model allows one to compare the effect of the resonant state on DOS, m_D^* , and S , to the effect of increase in band degeneracy, N_V . When a single valence band has N_V extremes inside the first Brillouin zone ($N_V = 4$ in PbTe for the L -point band and $N_V = 12$ for the Σ band), the DOS effective mass increases $N_V^{2/3}$ times. Thus, to get a comparable increase of m_D^* as between PbTe:Na and PbTe:Tl (before reaching the Σ band), a degeneracy in PbTe:Tl would have to increase 2–3 times. This effect is realized in the resonant system by the shift of states from the deeper energy range to the region near E_F , and, crucially, without forming an additional impurity band.

The second simplified explanation for the increase in thermopower may be formulated after plotting the $\ln \sigma(E)$ curves, which is done in Fig. 14. As $S \propto -d \ln \sigma(E) / dE$, the steeper is the $\ln \sigma(E)$ function, the larger is the thermopower. A first look at the conductivity curves in Fig. 11 may suggest that the Mott formula favors the PbTe:Na case. However, if we plot $\ln \sigma(E)$ as a function of the reduced energy, $E - \mu$, where μ is the chemical potential, the steeper character of the Tl-doped case around μ becomes visible. In Fig. 14, the chemical potential is

computed at $T = 300$ K for the nominal carrier concentrations of the studied systems.

IV. SUMMARY

In summary, we have studied the electronic structure and transport properties of 2% Tl-doped PbTe, 1% Na-doped PbTe, and the $\text{Cu}_{0.60}\text{Ni}_{0.40}$ alloy, using the KKR-CPA method and Kubo transport formalism. The characteristic distortions of the electronic structures, due to the presence of resonant levels in PbTe:Tl and Cu-Ni alloys as well as a rigid-band-like behavior of Na in PbTe, were evidenced by the computed Bloch spectral functions and densities of states. For Tl-doped PbTe, the self-compensation model was tested in calculations in which the tellurium vacancies are responsible for the reduction of the hole concentration in the samples. Ground-state transport functions $\sigma(E)$ of the studied systems, which take into account the impurity-induced scattering, were computed in the framework of Kubo formalism.

The obtained residual resistivities ρ_0 remain in a fairly good agreement with experimental ones in all of the studied materials, and show the increase of ρ_0 in PbTe:Tl versus PbTe:Na due to the presence of RL. This, independently of the thermoelectric properties, confirms the existence of the resonant state on Tl atoms. Moreover, analysis of ρ_0 as a function of Te vacancy concentration in $\text{Pb}_{0.98}\text{Tl}_{0.02}\text{Te}_{1-y}\text{Vac}_y$ gives credence to the self-compensation model since, without the shift of E_F induced by n -type vacancies, the computed ρ_0 would be too small. Thermopower was next computed using the $T = 0$ K transport functions and a perfect agreement with experiment for the Cu-Ni alloy was found. For PbTe, the calculated thermopowers are overestimated above $p = 10^{19} \text{ cm}^{-3}$, most likely due to inaccuracy of the Σ band position and effective mass overestimation, both related to the local density approximation treatment of the exchange and correlation effects. However, a relative increase in thermopower due to the presence of the resonant state is confirmed, giving a 50–100 $\mu\text{V/K}$ larger room-temperature thermopower in PbTe:Tl than in PbTe:Na in the same carrier concentration range. The increase in S may be qualitatively understood in terms of the increase in the density-of-states effective mass. Alternatively, in some sense, RL works in a similar way as the increase in band degeneracy: no additional impurity band is formed in PbTe:Tl, but the number of electronic states around the pristine PbTe valence band increases due to the presence of the resonant state.

ACKNOWLEDGMENTS

This work was partly supported by the National Science Center (Poland), Grant No. 2017/26/E/ST3/00119, and by the AGH-UST statutory tasks, Grant No. 11.11.220.01/5, within subsidy of the Ministry of Science and Higher Education.

APPENDIX A: PISARENKO CURVE FOR PBTE:NA

To verify the accuracy of the thermopower calculations for PbTe:Na in the lower doping regime, calculations of the transport properties of $\text{Pb}_{0.995}\text{Na}_{0.005}\text{Te}$ system were done and S was computed in the same way as described above for

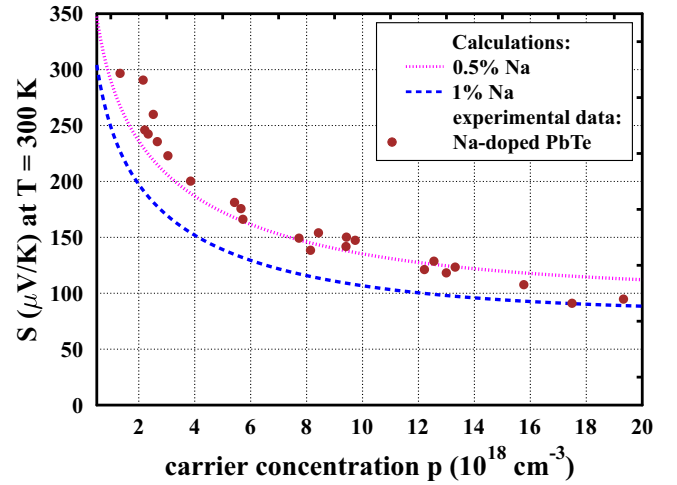


FIG. 15. Calculated Pisarenko curve for $\text{Pb}_{0.99}\text{Na}_{0.01}\text{Te}$ and $\text{Pb}_{0.995}\text{Na}_{0.005}\text{Te}$, compared with the experimental results (see Fig. 12 for references). In the lower doping regime, calculations for 0.5% Na-doped PbTe better reproduce the experimental trend and correct the deviation seen at lower p in Fig. 12.

$\text{Pb}_{0.99}\text{Na}_{0.01}\text{Te}$. Figure 15 shows the Pisarenko curve between $5 \times 10^{17} \text{ cm}^{-3}$ and $2 \times 10^{19} \text{ cm}^{-3}$. Agreement between the experimental results and calculations is much better for the 0.5% Na case since naturally the smaller concentration of Na better represents the properties of a more lightly doped material. This shows that in terms of the transport properties, the rigid-band model is only “locally” valid in PbTe:Na, i.e., one should not extrapolate the theoretically calculated thermopower on carrier concentrations, which are smaller/larger by more than an order of magnitude from the nominal one.

Additionally, better agreement of S between our calculations and experiment for $p \sim 10^{18} \text{ cm}^{-3}$, where at room temperature the contribution from the Σ band is smaller, shows that the shift of the Σ band in DFT calculations is partly responsible for the overestimation of S , seen in our studies for higher p .

APPENDIX B: m_D^* FORMULA

Below we give the derivation of the DOS effective mass formula (5). For the free-electron gas, the density of states $n(E)$ for a single parabolic band is given as [88]

$$n(E) = \frac{m_e^{3/2} V}{\pi^2 \hbar^3} \sqrt{2E}, \quad (\text{B1})$$

where $n(E)$ is in (states/energy) units, per two spin directions, and V is the unit-cell volume. The energy derivative of $n(E)$ is

$$n'(E) \equiv \frac{\partial n(E)}{\partial E} = \frac{m_e^{3/2} V}{\pi^2 \hbar^3} \frac{1}{\sqrt{2E}}. \quad (\text{B2})$$

By multiplying Eqs. (B1) and (B2), we get

$$n'(E)n(E) = \frac{m_e^3 V^2}{\pi^4 \hbar^6}. \quad (\text{B3})$$

Now, extracting the mass, one has

$$m_e = \hbar^2 \sqrt[3]{\pi^4 n(E) n'(E) / V^2}. \quad (\text{B4})$$

If, instead of the parabolic free-electron band with $n(E) \propto \sqrt{E}$, one has a nonparabolic band, formula (B4) may be used to obtain an energy-dependent density of states effective mass, which in m_e units will be given as

$$m_D^* = \frac{\hbar^2}{m_e} \sqrt[3]{\pi^4 n(E) n'(E) / V^2}. \quad (\text{B5})$$

If DOS is calculated in atomic Rydberg units (1/Ry), where $\hbar = 1$, $2m_e = 1$, the formula is further simplified,

$$m_D^* = 2 \sqrt[3]{\pi^4 n(E) n'(E) / V^2}, \quad (\text{B6})$$

where V has to be given in atomic a_B^3 units, where $a_B \simeq 0.529 \text{ \AA}$ is the Bohr radius. This formula gives an easy and direct way of obtaining the single-band DOS effective mass, with no need to fit the DOS function, and was already successfully applied to Mg_2X , SnSe , and tetradymites Bi_2Te_3 , Bi_2Se_3 , and Sb_2Te_3 in Refs. [84,85,89].

-
- [1] B. L. Györffy and G. M. Stocks, First principles band theory for random metallic alloys, in *Electrons in Disordered Metals and at Metallic Surfaces*, NATO ASI Series, edited by P. Phariseau, B. L. Györffy, and L. Scheire (Springer-Verlag, New York, 1979).
- [2] J. P. Heremans, B. Wiendlocha, and A. M. Chamoire, Resonant levels in bulk thermoelectric semiconductors, *Energy Environ. Sci.* **5**, 5510 (2012).
- [3] F. J. Blatt, P. A. Schroeder, C. L. Foiles, and D. Greig, *Thermoelectric Power of Metals* (Plenum, New York, 1976).
- [4] A. N. Gerritsen and J. Koringa, Anomalous resistance of noble metals containing paramagnetic ions, *Phys. Rev.* **84**, 604 (1951).
- [5] J. Koringa and A. N. Gerritsen, The cooperative electron phenomenon in dilute alloys, *Physica* **19**, 457 (1953).
- [6] J. Friedel, On some electrical and magnetic properties of metallic solid solutions, *Can. J. Phys.* **34**, 1190 (1956).
- [7] J. P. Heremans, V. Jovovic, E. S. Toberer, A. Saramat, K. Kurosaki, A. Charoenphakdee, S. Yamanaka, and G. J. Snyder, Enhancement of thermoelectric efficiency in PbTe by distortion of the electronic density of states, *Science* **321**, 554 (2008).
- [8] I. A. Chernik and S. N. Lykov, Superconductivity of PbTe doped with Tl - valent band density of states of PbTe doped with Tl and Na, *Sov. Phys. Solid State* **23**, 1724 (1981).
- [9] S. A. Kaz'min, S. N. Lykov, R. V. Parfen'ev, I. K. Chernik, and D. V. Shamshur, Critical-temperature dependence on hole concentration in PbTe(Tl), *Sov. Phys. Solid State* **24**, 832 (1982).
- [10] V. I. Kaidanov and Yu. I. Ravich, Deep and resonance states in A IV B VI semiconductors, *Sov. Phys. Usp.* **28**, 31 (1985).
- [11] S. A. Nemov and Yu. I. Ravich, Thallium dopant in lead chalcogenides: Investigation methods and peculiarities, *Phys. Usp.* **41**, 735 (1998).
- [12] Y. Matsushita, P. A. Wiannecki, A. T. Sommer, T. H. Geballe, and I. R. Fisher, Type II superconducting parameters of Tl-doped PbTe determined from heat capacity and electronic transport measurements, *Phys. Rev. B* **74**, 134512 (2006).
- [13] Y. Matsushita, H. Bluhm, T. H. Geballe, and I. R. Fisher, Evidence for Charge Kondo Effect in Superconducting Tl-Doped PbTe, *Phys. Rev. Lett.* **94**, 157002 (2005).
- [14] T. A. Costi and V. Zlatić, Charge Kondo Anomalies in PbTe Doped with Tl Impurities, *Phys. Rev. Lett.* **108**, 036402 (2012).
- [15] H. Mukuda, T. Matsumura, S. Maki, M. Yashima, Y. Kitaoka, K. Miyake, H. Murakami, P. Giraldo-Gallo, T. H. Geballe, and I. R. Fisher, Anomalous ^{125}Te nuclear spin relaxation coincident with charge kondo behavior in superconducting $\text{Pb}_{1-x}\text{Tl}_x\text{Te}$, *J. Phys. Soc. Jpn.* **87**, 023706 (2018).
- [16] B. Wiendlocha, Resonant levels, vacancies, and doping in Bi_2Te_3 , $\text{Bi}_2\text{Te}_2\text{Se}$, and Bi_2Se_3 tetradymites, *J. Electron. Mater.* **45**, 3515 (2016).
- [17] S. Kim, B. Wiendlocha, H. Jin, J. Tobola, and J. P. Heremans, Electronic structure and thermoelectric properties of p-type Ag-doped Mg_2Sn and $\text{Mg}_2\text{Sn}_{1-x}\text{Si}_x$ ($x = 0.05, 0.1$), *J. Appl. Phys.* **116**, 153706 (2014).
- [18] P. Nieroda, K. Kutorasinski, J. Tobola, and K. T. Wojciechowski, Search for resonant-like impurity in Ag-doped CoSb_3 skutterudite: Theoretical and experimental study, *J. Electron. Mater.* **43**, 1681 (2014).
- [19] C. M. Jaworski, V. Kulbachinskii, and J. P. Heremans, Resonant level formed by tin in Bi_2Te_3 and the enhancement of room-temperature thermoelectric power, *Phys. Rev. B* **80**, 233201 (2009).
- [20] Q. Zhang, B. Liao, Y. Lan, K. Lukas, W. Liu, K. Esfarjani, C. Opeil, D. Broido, G. Chen, and Z. Ren, High thermoelectric performance by resonant dopant indium in nanostructured SnTe, *Proc. Natl. Acad. Sci. USA* **110**, 13261 (2013).
- [21] L. Wu, X. Li, S. Wang, T. Zhang, J. Yang, W. Zhang, L. Chen, and J. Yang, Resonant level-induced high thermoelectric response in indium-doped GeTe, *Npg Asia Mater.* **9**, e343 (2017).
- [22] J. P. Heremans, B. Wiendlocha, and H. Jin, Thermoelectric Materials with Resonant States, in *Advanced Thermoelectrics: Materials, Contacts, Devices, and Systems*, edited by Zhifeng Ren, Yucheng Lan, and Qinyong Zhang (Taylor and Francis, Boca Raton, FL, 2018).
- [23] B. Paul and P. Banerji, The effect of chromium impurity on the thermoelectric properties of PbTe in the temperature range 100-600 K, *J. Appl. Phys.* **109**, 103710 (2011).
- [24] B. Paul, P. K. Rawat, and P. Banerji, Dramatic enhancement of thermoelectric power factor in PbTe:Cr co-doped with iodine, *Appl. Phys. Lett.* **98**, 262101 (2011).
- [25] E. Grodzicka, W. Dobrowolski, J. Kossut, T. Story, and B. Witkowska, Peculiarities of transport properties in semiconductors with resonant impurities: HgSe: Fe versus PbTe: Cr, *J. Cryst. Growth* **138**, 1034 (1994).
- [26] M. D. Nielsen, E. M. Levin, C. M. Jaworski, K. Schmidt-Rohr, and J. P. Heremans, Chromium as resonant donor impurity in PbTe, *Phys. Rev. B* **85**, 045210 (2012).
- [27] T. Story, E. Grodzicka, B. Witkowska, J. Górecka, and W. Dobrowolski, Transport and magnetic properties of PbTe:Cr and PbSnTe:Cr, *Acta Phys. Pol. A* **82**, 879 (1992).
- [28] D. T. Morelli, J. P. Heremans, and C. M. Thrush, Magnetic and thermal properties of iron-doped lead telluride, *Phys. Rev. B* **67**, 035206 (2003).
- [29] E. P. Skipetrov, O. V. Kruleveckaya, L. A. Skipetrova, E. I. Slynko, and V. E. Slynko, Fermi level pinning in Fe-doped PbTe under pressure, *Appl. Phys. Lett.* **105**, 022101 (2014).

- [30] E. P. Skipetrov, L. A. Skipetrova, A. V. Knotko, E. I. Slynko, and V. E. Slynko, Scandium resonant impurity level in PbTe, *J. Appl. Phys.* **115**, 133702 (2014).
- [31] J. D. König, M. D. Nielsen, Y.-B. Gao, M. Winkler, A. Jacquot, H. Böttner, and J. P. Heremans, Titanium forms a resonant level in the conduction band of PbTe, *Phys. Rev. B* **84**, 205126 (2011).
- [32] B. Wiendlocha, Localization and magnetism of the resonant impurity states in Ti doped PbTe, *Appl. Phys. Lett.* **105**, 133901 (2014).
- [33] B. Wiendlocha, Fermi surface and electron dispersion of PbTe doped with resonant Tl impurity from KKR-CPA calculations, *Phys. Rev. B* **88**, 205205 (2013).
- [34] B. Wiendlocha, K. Kutorasinski, S. Kaprzyk, and J. Tobola, Recent progress in calculations of electronic and transport properties of disordered thermoelectric materials, *Scr. Mater.* **111**, 33 (2016).
- [35] M. Matusiak, E. M. Tunnicliffe, J. R. Cooper, Y. Matsushita, and I. R. Fisher, Evidence for a charge Kondo effect in $\text{Pb}_{1-x}\text{Ti}_x\text{Te}$ from measurements of thermoelectric power, *Phys. Rev. B* **80**, 220403 (2009).
- [36] H. Ebert *et al.*, The Munich SPR-KKR package, version 6.3.1. and 7.7.1. <http://ebert.cup.uni-muenchen.de/SPRKKR> (2012).
- [37] H. Ebert, D. Ködderitzsch, and J. Minár, Calculating condensed matter properties using the KKR-Green's function method - recent developments and applications, *Rep. Prog. Phys.* **74**, 096501 (2011).
- [38] S. H. Vosko, L. Wilk, and M. Nusair, Accurate spin-dependent electron liquid correlation energies for local spin density calculations: A critical analysis, *Can. J. Phys.* **58**, 1200 (1980).
- [39] Yu. I. Ravich, B. A. Efimova, and I. A. Smirnov, *Semiconducting Lead Chalcogenides* (Plenum, New York, 1970).
- [40] C. L. Foiles, Electrical resistivity, thermoelectrical power and optical properties Figs. 67-98: Datasheet from Landolt-Börnstein - group iii condensed matter volume 15b: "electrical resistivity, thermoelectrical power and optical properties" in *Springer-materials* (http://dx.doi.org/10.1007/10201705_25) (Springer-Verlag, Berlin, 1985).
- [41] H. Ebert, A. Vernes, and J. Banhart, Relativistic bandstructure of disordered magnetic alloys, *Solid State Commun.* **104**, 243 (1997).
- [42] J. S. Faulkner and G. M. Stocks, Calculating properties with the coherent-potential approximation, *Phys. Rev. B* **21**, 3222 (1980).
- [43] B. E. A. Gordon, W. E. Temmerman, and B. L. Gyorffy, On the Fermi surfaces of paramagnetic $\text{Cu}_c\text{Ni}_{1-c}$ alloys, *J. Phys. F* **11**, 821 (1981).
- [44] W. H. Butler, Theory of electronic transport in random alloys: Korringa-Kohn-Rostoker coherent-potential approximation, *Phys. Rev. B* **31**, 3260 (1985).
- [45] W. H. Butler and G. M. Stocks, Calculated electrical conductivity and thermopower of silver-palladium alloys, *Phys. Rev. B* **29**, 4217 (1984).
- [46] R. Kubo, Statistical-Mechanical Theory of Irreversible Processes. I. General Theory and Simple Applications to Magnetic and Conduction Problems, *J. Phys. Soc. Jpn.* **12**, 570 (1957).
- [47] D. A. Greenwood, The boltzmann equation in the theory of electrical conduction in metals, *Proc. Phys. Soc.* **71**, 585 (1958).
- [48] J. C. Swihart, W. H. Butler, G. M. Stocks, D. M. Nicholson, and R. C. Ward, First-Principles Calculation of the Residual Electrical Resistivity of Random Alloys, *Phys. Rev. Lett.* **57**, 1181 (1986).
- [49] D. Ködderitzsch, S. Lowitzer, J. B. Staunton, and H. Ebert, Electronic and transport properties of disordered transition-metal alloys, *Phys. Status Solidi B* **248**, 2248 (2011).
- [50] V. Popescu, P. Kratzer, S. Wimmer, and H. Ebert, Native defects in the Co_2TiZ ($Z = \text{Si, Ge, Sn}$) full Heusler alloys: Formation and influence on the thermoelectric properties, *Phys. Rev. B* **96**, 054443 (2017).
- [51] J. Banhart and H. Ebert, First-principles theory of spontaneous-resistance anisotropy and spontaneous Hall effect in disordered ferromagnetic alloys, *Europhys. Lett.* **32**, 517 (1995).
- [52] H. Ebert, A. Vernes, and J. Banhart, Anisotropic electrical resistivity of ferromagnetic Co-Pd and Co-Pt alloys, *Phys. Rev. B* **54**, 8479 (1996).
- [53] J. Banhart, H. Ebert, P. Weinberger, and J. Voithländer, Approximations made in evaluating the residual electrical dc resistivity of disordered alloys, *Phys. Rev. B* **50**, 2104 (1994).
- [54] J. Banhart and H. Ebert, First-principles calculation of the thermoelectric power of disordered alloys, *Solid State Commun.* **94**, 445 (1995).
- [55] A. Vernes, H. Ebert, and J. Banhart, Electronic conductivity in $\text{Ni}_x\text{Cr}_{1-x}$ and $\text{Ni}_x\text{Cu}_{1-x}$ fcc alloy systems, *Phys. Rev. B* **68**, 134404 (2003).
- [56] I. Turek and T. Záležák, Residual resistivity and its anisotropy in random CoNi and CuNi ferromagnetic alloys, *J. Phys.: Conf. Ser.* **200**, 052029 (2010).
- [57] C. Y. Ho, M. W. Ackerman, K. Y. Wu, S. G. Oh, and T. N. Havill, Thermal conductivity of ten selected binary alloy systems, *J. Phys. Chem. Ref. Data* **7**, 959 (1978).
- [58] G. M. Stocks and W. H. Butler, Mass and Lifetime Enhancement due to Disorder on $\text{Ag}_c\text{Pd}_{1-c}$ Alloys, *Phys. Rev. Lett.* **48**, 55 (1982).
- [59] J. Mao, Y. Wang, H. Seok Kim, Z. Liu, U. Saparamadu, F. Tian, K. Dahal, J. Sun, S. Chen, W. Liu, and Z. Ren, High thermoelectric power factor in Cu-Ni alloy originate from potential barrier scattering of twin boundaries, *Nano Energy* **17**, 279 (2015).
- [60] C. M. Jaworski, B. Wiendlocha, V. Jovovic, and J. P. Heremans, Combining alloy scattering of phonons and resonant electronic levels to reach a high thermoelectric figure of merit in PbTeSe and PbTeS alloys, *Energy Environ. Sci.* **4**, 4155 (2011).
- [61] S. Ahmad, K. Hoang, and S. D. Mahanti, Ab Initio Study of Deep Defect States in Narrow Band-Gap Semiconductors: Group III Impurities in PbTe, *Phys. Rev. Lett.* **96**, 056403 (2006).
- [62] K. Hoang and S. D. Mahanti, Electronic structure of Ga-, In-, and Tl-doped PbTe: A supercell study of the impurity bands, *Phys. Rev. B* **78**, 085111 (2008).
- [63] Y. Takagiwa, Y. Pei, G. Pomrehn, and G. J. Snyder, Validity of rigid band approximation of PbTe thermoelectric materials, *APL Mater.* **1**, 011101 (2013).
- [64] H. Jin, B. Wiendlocha, and J. P. Heremans, P-type doping of elemental bismuth with indium, gallium and tin: A novel doping mechanism in solids, *Energy Environ. Sci.* **8**, 2027 (2015).
- [65] T. Keiber, F. Bridges, B. C. Sales, and H. Wang, Complex role for thallium in PbTe:Tl from local probe studies, *Phys. Rev. B* **87**, 144104 (2013).

- [66] S. D. Waddington, P. Weightman, and A. D. C. Grassie, The charge state of Tl impurities in PbTe, *J. Phys. C* **21**, 2695 (1988).
- [67] F. Bridges, T. Keiber, S. Medling, and B. C. Sales, Unusual distortions about Tl and Pb in PbTe:Tl, *Phys. Status Solidi C* **10**, 236 (2013).
- [68] A. Dewandre, O. Hellman, S. Bhattacharya, A. H. Romero, G. K. H. Madsen, and M. J. Verstraete, Two-Step Phase Transition in SnSe and the Origins of its High Power Factor from First Principles, *Phys. Rev. Lett.* **117**, 276601 (2016).
- [69] M.-S. Lee and S. D. Mahanti, Validity of the rigid band approximation in the study of the thermopower of narrow band gap semiconductors, *Phys. Rev. B* **85**, 165149 (2012).
- [70] P. Giraldo-Gallo, P. Walmsley, B. Sangiorgio, S. C. Riggs, R. D. McDonald, L. Buchauer, B. Fauque, C. Liu, N. A. Spaldin, A. Kaminski, K. Behnia, and I. R. Fisher, Evidence of incoherent carriers associated with resonant impurity levels and their influence on superconductivity in the anomalous superconductor $\text{Pb}_{1-x}\text{Tl}_x\text{Te}$, [arXiv:1711.05723](https://arxiv.org/abs/1711.05723).
- [71] Strictly speaking, $L(E)$ was fitted in the atomic units, i.e., with Ry units on the energy axis of Fig. 8, which guarantees that the area under BSF is equal to 2.0 (the occupation of each electronic state), with the factor 2 coming from the spin degeneracy.
- [72] Y. Matsushita, Superconductivity and mixed valency in thallium-doped lead telluride, Ph.D. thesis, Stanford University, 2007.
- [73] C. M. Jaworski, M. D. Nielsen, H. Wang, S. N. Girard, W. Cai, W. D. Porter, M. G. Kanatzidis, and J. P. Heremans, Valence-band structure of highly efficient p -type thermoelectric PbTe-PbS alloys, *Phys. Rev. B* **87**, 045203 (2013).
- [74] Uncertainty of the measured resistivity was either given in the reference work or estimated based on a point size in the published figures.
- [75] Y. Pei, A. LaLonde, S. Iwanaga, and G. J. Snyder, High thermoelectric figure of merit in heavy hole dominated PbTe, *Energy Environ. Sci.* **4**, 2085 (2011).
- [76] It is worth noting that the proportionality $\sigma(E) \propto n(E)$ is not linear; $\sigma(E)$ increases faster than DOS when E goes deeper into the VB, and $\sigma(E)/n(E)$ has the same trend, with $\sigma(E)/n(E) \propto \ln(E_V - E)$ near the VB edge. In the Na-doped case, the situation is opposite and $\sigma(E)/n(E)$ decreases when moving away from the band edge, i.e., DOS grows faster than $\sigma(E)$.
- [77] S. V. Airapetyants, M. N. Vinograd, I. N. Dubrovsk, N. V. Kolomoet, and I. M. Rudnik, Structure of the valence band of heavily doped lead telluride, *Sov. Phys. Solid State* **8**, 1069 (1966).
- [78] A. J. Crocker and L. M. Rogers, Interpretation of the hall coefficient, electrical resistivity and Seebeck coefficient of P -type lead telluride, *Br. J. Appl. Phys.* **18**, 563 (1967).
- [79] I. A. Chernik, V. I. Kaidanov, M. I. Vinogradova, and N. V. Kolomoets, Investigation of the valence band of lead telluride using transport phenomena, *Sov. Phys. Semiconduct.* **2**, 645 (1968).
- [80] D. J. Singh, Doping-dependent thermopower of PbTe from Boltzmann transport calculations, *Phys. Rev. B* **81**, 195217 (2010).
- [81] K. Berland and C. Persson, Thermoelectric transport of GaAs, InP, and PbTe: Hybrid functional with $k \cdot p$ interpolation versus scissor-corrected generalized gradient approximation, [arXiv:1803.07854](https://arxiv.org/abs/1803.07854).
- [82] P. Giraldo-Gallo, B. Sangiorgio, P. Walmsley, H. J. Silverstein, M. Fechner, S. C. Riggs, T. H. Geballe, N. A. Spaldin, and I. R. Fisher, Fermi surface evolution of Na-doped PbTe studied through density functional theory calculations and Shubnikov-de Haas measurements, *Phys. Rev. B* **94**, 195141 (2016).
- [83] J. D. Jensen, B. Houston, and J. R. Burke, Fermi-surface parameters of p -type PbTe as a function of carrier density, *Phys. Rev. B* **18**, 5567 (1978).
- [84] K. Kutorasinski, B. Wiendlocha, J. Tobola, and S. Kaprzyk, Importance of relativistic effects in electronic structure and thermopower calculations for Mg_2Si , Mg_2Ge , and Mg_2Sn , *Phys. Rev. B* **89**, 115205 (2014).
- [85] K. Kutorasinski, B. Wiendlocha, S. Kaprzyk, and J. Tobola, Electronic structure and thermoelectric properties of n - and p -type SnSe from first-principles calculations, *Phys. Rev. B* **91**, 205201 (2015).
- [86] Experimental DOS effective mass m_D^* is recalculated based on the measured transverse cyclotron effective masses m_{\perp}^{cyc} and anisotropy parameter K , given in Refs. [82,83], from which we get $m_{\parallel}^{\text{cyc}} = \sqrt{K} m_{\perp}^{\text{cyc}}$. In terms of the band effective masses m^* , $m_{\perp}^{\text{cyc}} = m_{\perp}^*$, $m_{\parallel}^{\text{cyc}} = \sqrt{m_{\perp}^* m_{\parallel}^*}$, where symbols \perp and \parallel refer to the directions perpendicular and parallel to the semimajor axis, respectively, of the L -pocket ellipsoid (see Ref. [82] for details). From that, we get $m_D^* = N_V^{2/3} \sqrt[3]{m_{\perp}^{*2} m_{\parallel}^*} = N_V^{2/3} \sqrt[3]{K(m_{\perp}^{\text{cyc}})^3}$, where $N_V = 4$ is the number of L pockets.
- [87] Heremans *et al.* [7] show that the temperature-dependent effective mass and carrier concentration points in Fig. 13 correspond to their data for $T = 77, 200$, and 300 K. Jaworski *et al.* [60] give m_D^* values for $T = 77$ and $T = 300$ K, where slightly different carrier concentrations were recorded.
- [88] C. Kittel, *Introduction to Solid State Physics*, 8th ed. (Wiley, New York, 2004).
- [89] J. P. Heremans and B. Wiendlocha, Tetradymites: Bi_2Te_3 -Related Materials, in *Materials Aspect of Thermoelectricity*, edited by C. Uher (Taylor and Francis, Boca Raton, FL, 2017).